

A Comparative Study on Ni-Based Coatings Prepared by HVAF, HVOF, and APS Methods for Corrosion Protection Applications

E. Sadeghimeresht, N. Markocsan, and P. Nylén

(Submitted June 8, 2016; in revised form October 16, 2016)

Selection of the thermal spray process is the most important step toward a proper coating solution for a given application as important coating characteristics such as adhesion and microstructure are highly dependent on it. In the present work, a process-microstructure-properties-performance correlation study was performed in order to figure out the main characteristics and corrosion performance of the coatings produced by different thermal spray techniques such as high-velocity air fuel (HVAF), high-velocity oxy fuel (HVOF), and atmospheric plasma spraying (APS). Previously optimized HVOF and APS process parameters were used to deposit Ni, NiCr, and NiAl coatings and compare with HVAF-sprayed coatings with randomly selected process parameters. As the HVAF process presented the best coating characteristics and corrosion behavior, few process parameters such as feed rate and standoff distance (SoD) were investigated to systematically optimize the HVAF coatings in terms of low porosity and high corrosion resistance. The Ni and NiAl coatings with lower porosity and better corrosion behavior were obtained at an average SoD of 300 mm and feed rate of 150 g/min. The NiCr coating sprayed at a SoD of 250 mm and feed rate of 75 g/min showed the highest corrosion resistance among all investigated samples.

Keywords corrosion, OCP, process optimization, potentiodynamic polarization, thermal spraying

1. Introduction

Ni-based coatings such as Ni, NiCr, and NiAl coatings are extensively used to repair or protect structural materials in corrosive environments (Ref 1-5). Corrosion protection requires coatings with dense microstructure and high adherence in order to insulate the substrate material from the surrounding corrosion environment (Ref 6-8). Addition of alloying elements such as Cr or Al to these materials facilitates a passivation layer formation that improves the corrosion resistance of the coatings (Ref 9, 10). A dense coating with uniform microstructure and less defects is not only hindering the corrosive agent penetration, but also helps to a quicker passive layer formation as pores are considered as barriers for rapid diffusion of the passive layer-forming elements. Typically, a pore, particularly if connected to other pores, allows much faster penetration of the electrolyte solution inside the coating and toward the substrate and acts as a crevice to hinder proper passivation of the metal alloy along its surfaces (Ref 11). It is well known that the thermal spray methods are mostly defined by their in-flight particle

characteristics, i.e., temperature and velocity, which in turn have the highest influence on coatings microstructure. Comparing high-velocity air fuel (HVAF), high-velocity oxy fuel (HVOF), and atmospheric plasma spraying (APS), they have, in this order, decreasing spraying velocity and increasing spraying temperature hence obviously different specific microstructures (Ref 12). Selection of a right material and an appropriate thermal spray method regarding the target application is of high interest in order to attain an effective coating microstructure in corrosive environment.

Ni-based coatings have been deposited by several techniques, e.g., electron beam physical vapor deposition (EB-PVD) (Ref 13), vacuum and air plasma spray (VPS and APS) (Ref 14, 15), HVOF (Ref 16), and more recently HVAF (Ref 17). By the latter, metallic alloy coating could be dense and uniform with high adhesion/cohesion strength with almost no oxide content owing to the high kinetic energy and relatively low temperature of the feedstock powder injected into the flame (Ref 18). HVAF process has been widely employed to produce coatings to protect critical components used in industrial applications with aggressive environments (Ref 19-21).

Compared to HVOF, which is a technique based on tunable combustion gas parameters for a fixed hardware design, HVAF is mostly a hardware-based configuration; therefore, for instance, the gas flow rate is not effective for changing the spray conditions. The most important factors in tuning the HVAF process are: (1) hardware configuration such as the size of the combustion chamber, nozzle, and powder injector and (2) process variables such as

E. Sadeghimeresht, N. Markocsan, and P. Nylén, Department of Engineering Science, University West, 461 53 Trollhättan, Sweden. Contact e-mail: esmaeil.sadeghimeresht@hv.se.



standoff distance (SoD) and powder feed rate (Ref 22-28). Regardless the preliminary development of spray conditions specific to a given powder chemistry, systematic optimization of HVAF process itself has been scarcely performed. Indeed, in order to spray coatings with required corrosion performance, systematic process parameter analysis must be applied to relate the applied parameters with the produced coating structure and properties (Ref 29). The process-microstructure-properties-performance relationship assessment is a capable tool for process optimization and able to provide precise information of the whole process from the powder to coating performance (Ref 30, 31).

In this study, HVOF-, APS-, and HVAF-sprayed Ni, NiCr, and NiAl coatings were comparatively investigated in order to understand the microstructural features' effect on corrosion mechanisms and evaluate the diffusion paths of alloying elements such as Cr and Al to form a passivation layer in different spraying systems. The microstructure of the HVAF coatings was further optimized in order to obtain least porous coatings suitable for corrosion protection applications. The microstructure and corrosion properties of the coating were analyzed using SEM/EDS, XRD, and electrochemical corrosion techniques to form a link among the spraying processes, microstructure, and corrosion behavior.

2. Experimental Procedure

2.1 Substrate

Coupon-shaped ($\phi = 25.5$ mm and thickness = 6 mm) specimens of structural low-carbon steel Domex 355 (chemical composition in wt.%; 0.10C-0.03Si-1.5Mn-0.02P-0.01S-0.2V-0.15Ti) were used as the substrate material, which were fixed on a rotating carousel and sprayed. Prior to spraying, the substrates were grit-blasted to be cleaned and roughened to a surface roughness (R_a) of around 6 μm using the HVAF spray gun with standard configuration (long nozzle, large combustion chamber, short axial powder injector, and propane as a combustion gas). The used grit media is DURALUM White F220 aluminum oxide powder mesh 220. The samples' surface was not altered (no machining) after spraying in order to determine their functional performances in the as-sprayed state (a technical solution which is more relevant for industrial applications). Before each corrosion test, the as-sprayed samples were degreased and rinsed in high-purity water, followed by ethanol/air-drying.

2.2 Feedstock Materials

Three commercial powders of Ni (Amperit 176.001, H.C. Starck), NiCr (Amperit 251.001, H.C. Starck), and NiAl (Amperit 281.003, H.C. Starck) were selected for this study. The chemical composition, particle size distribution, and density of the powders are given in Table 1. All powders are gas-atomized with a spheroidal morphology, as shown in Fig. 1. An optimum particle size with

narrow size distribution and spherical-shaped powders were shown as key requirement to obtain a coating as dense as possible in thermal spray processes (Ref 32).

2.3 Solution Preparation

Corrosion experiments were operated in 3.5 wt.% NaCl solution. The solution was prepared from analytical-grade reagents using distilled water. All the experiments were performed under thermostatic conditions (24 ± 0.1 °C), while the solution was in equilibrium with the surrounding atmosphere.

2.4 APS, HVAF, and HVOF Spraying

The samples in this study were sprayed by APS, HVOF, and HVAF techniques. The spray equipment used are F4-MB APS plasma gun (Sulzer Metco, Westbury, NY, USA), a DJ2600 Hybrid HVOF gun (Sulzer Metco, Westbury, NY, USA), and a HVAF system equipped with a M3 gun (Uniquocoat M3™, Oilville, VA, USA). The characteristics components of the HVAF gun are a long axial powder injector, a short combustion chamber, and a de Laval nozzle with a length of 250 mm. The spray parameters for all spraying methods of the three powders are given in Tables 2, 3, 4, 5, and 6.

2.5 Characterization Methods

2.5.1 Porosity, Microhardness, and Surface Roughness Measurements. After metallographic preparation, the as-sprayed samples were subjected to porosity measurement using an image analyzer with ImageJ software based on ASTM standard B276 (Ref 33) by converting the gray scale micrographs (taken with an Olympus BX60M optical microscope) into binary images and quantifying the percentage of dark areas in these images. Three optical micrographs were used for each coating to measure the pore content.

The surface roughness of the coatings was measured with a stylus-based profilometer (Surface 301, Mitutoyo, Kanagawa, Japan).

Micro-Vickers hardness measurements were performed using a Microhardness Tester (HMV-2, Shimadzu, Tokyo, Japan) on the polished cross section of the coatings according to the ASTM standard E384 (Ref 34). A Vickers indenter with a load of 300 g and dwell time of 15 s. $HV_{0.3}$ was used in this study. Average values of 20 indentations were calculated for each sample.

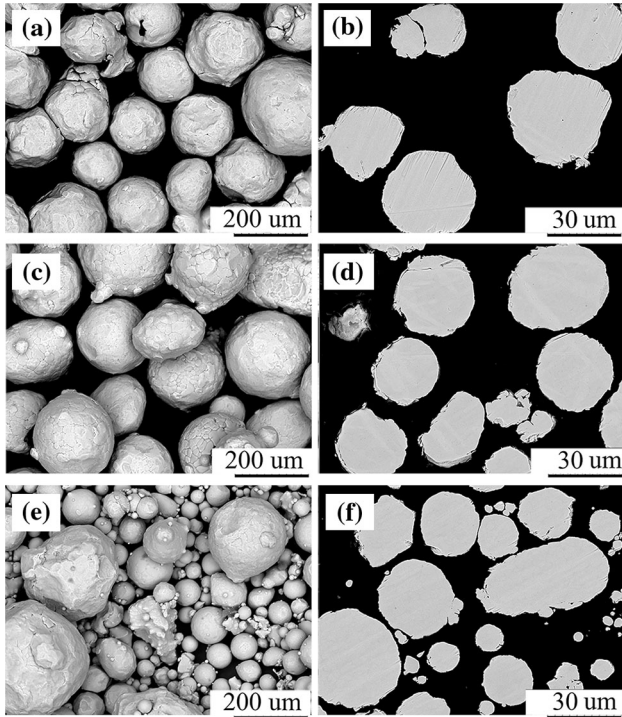
2.5.2 Phase Analysis. X-ray diffraction analysis of powder feedstock and coated systems was carried out with a Siemens diffractometer (Kristalloflex D500, Siemens, Germany), using an X'Pert PRO diffractometer with $\text{Cu-K}\alpha$ ($\lambda = 0.154$ nm) radiation and a diffraction angle (2θ) between 20° and 80°.

2.6 Corrosion Tests; Open-Circuit Potential (OCP); and Potentiodynamic Polarization

Electrochemical measurements were performed in a three-electrode cell with the as-sprayed coating sample as the working electrode (WE), a saturated calomel reference

Table 1 Spraying powder characteristics

Powder	Chemical composition, wt.%				Apparent density, g/cm ³	Particle size distribution, μm		
	Ni	Cr	Al	O		D90%	D50%	D10%
Ni	Bal	0.1	3.4	26-39	19-24	10-15
NiCr	Bal	19.1	...	0.1	3.3	25-29	14-18	5-9
NiAl	Bal	...	5.5	0.1	3.7	25-29	14-18	5-9

**Fig. 1** Back-scattered SEM topographical and cross-sectional micrographs of the powders. (a, b) Ni, (c, d) NiCr, and (e, f) NiAl

electrode (SCE), and a platinum foil as counter electrode. All the potentials presented were referred to the reference electrode of SCE. The surface area exposed to the electrolyte was 0.2 cm².

Prior to each measurement, the samples were soaked in the electrolyte at the open-circuit potential for 3 h to obtain a stable state. The polarization curves were generated by scanning the potential range that varied from -250 to +2000 mV (versus OCP) at a scanning rate of 1.0 mV/s, using an IVIUMSTAT (IVIUM, Eindhoven, Netherlands) computer-controlled potentiostat/galvanostat. The Zview program was used for calculations of anodic (β_a) and cathodic (β_c) Tafel constants required for polarization resistance calculations. The polarization resistance (R_p) of the coating was calculated with the Stern-Geary Eq 1 (Ref 35):

$$R_p = \frac{dE}{di} = \frac{1}{i_{\text{corr}}} \frac{\beta_a \beta_c}{2.303(\beta_a + \beta_c)} \quad (\text{Eq 1})$$

where i_{corr} (A/cm) is the corrosion current density, β_a and β_c (V/dec) are the anodic and cathodic Tafel slopes, respectively.

3. Results and Discussion

3.1 Microstructural Characterization of As-Sprayed Coatings

3.1.1 APS Coatings. SEM cross-sectional micrographs of APS-sprayed coatings (Fig. 2) illustrate a clean coating/substrate interface without debonding and grit residues. The porosity level in the coatings was 1.7, 3.2, and 5.5 vol.% in Ni, NiCr, and NiAl coatings, respectively. Some dark oxide stringers [high-oxygen-containing regions (Ref 36)] were visible in the microstructure of the three coatings. The coatings were very porous and layered with numerous interlamellar pores; however, they were free of cracks or large pores. The coalesced splat/splat boundary is most probably due to metallic bonding and also the under-layer re-melting upon the arrival of a subsequent droplet (Ref 37). Based on the shape of the pores, it seems that the pores were likely formed due to the expansion of trapped air while the impacting particles were still molten. The other contributor to pore formation within the coatings could be the low kinetic energy of the particles in APS process (Ref 38). Another reason might be that large droplets heated well above the melting point can splash upon impact, projecting small satellite droplets, which become embedded in the coating as defects. Such rounded-edge particles, semi-melted, and solid particles of original powders were observed in the corresponding coating.

3.1.2 HVOF-Sprayed Coatings. Typical HVOF coating microstructures, comprising lamellar boundaries, semi- and fully melted particles, oxides, and pores, were observed in all the HVOF-sprayed samples. These microstructures are presented in Fig. 3. The coatings presented lower porosity, i.e., 0.9, 1.6, and 2.3 vol.% in Ni, NiCr, and NiAl coatings, respectively) compared to the APS-sprayed coatings which had almost double amounts of pores. No surface cracks in the coatings were detected. High level of cohesion between the splats was also observed at higher magnification ($\times 2000$).

There was a good contact of the coating with the substrate, suggesting a good bonding to the substrate.

In the HVOF coatings, the peening effect of previous sweeps is distinctive, as the coating structure seems to be much denser near the substrate, and the lamellar boundaries are more prominent in the surface layers of the coating (Ref 39).

The sharp irregular shapes of the small particles indicate that these particles were not melted during spraying.


Table 2 APS spraying process parameters

Coatings	Current, A	Voltage, V	Primary gas (Ar) flow, L/min	Secondary gas (H ₂) flow, L/min	Powder carrier gas (Ar) flow, L/min	Feed rate, g/min	Pass velocity, m/min	Pass spacing, mm/rev.	Thickness per pass, μm	Number of cycles	SoD, mm
Ni-P	600	65	55	10	3.5	50	75	4	31.8	8	140
NiCr-P	600	68	65	14	2.7	60	75	4	26.0	10	140
NiAl-P	600	66	45	11	2.5	50	75	4	33.1	8	140

Table 3 HVOF spraying process parameters

Coatings	O ₂ pressure, MPa	Fuel pressure, MPa	Air pressure, MPa	O ₂ flow, L/min	Fuel flow, L/min	Air flow, L/min	N ₂ flow, L/min	Feed rate, g/min	Pass velocity, m/min	Pass spacing, mm/rev.	Thickness per pass, μm	Number of cycles	SoD, mm
Ni-O	1.17	0.97	0.69	214	635	344	12.5	40	90	2	25.7	10	225
NiCr-O	1.17	0.97	0.69	214	635	344	12.5	40	90	2	22.8	11	225
NiAl-O	1.17	0.97	0.69	214	635	344	12.5	40	90	2	27.3	9	225

Table 4 HVAF spraying process parameters for Ni

Coatings	Nozzle	Air pressure, MPa	Fuel 1 pressure (propane), MPa	Fuel 2 pressure (propane), MPa	Powder carrier gas (N ₂) flow, L/min	Feed rate, g/min	Pass velocity, m/min	Pass spacing, mm/rev.	Thickness per pass, μm	Number of cycles	SoD, mm
Ni1	4L2G	0.8	0.69	0.69	60	150	100	5	40.1	6	300
Ni2	4L4G	0.83	0.69	0.69	60	150	100	5	46.7	6	300
Ni3	4L2G	0.8	0.69	0.69	60	75	100	5	27.5	9	350
Ni4	4L2G	0.8	0.69	0.69	60	75	100	5	25.5	10	300
Ni5	4L2G	0.8	0.69	0.69	60	75	100	5	25.2	10	250
Ni6	4L2G	0.8	0.69	0.69	60	150	100	5	57.1	7	400
Ni7	4L2G	0.8	0.69	0.69	60	75	100	5	26.4	10	400

Therefore, it can be assumed that a portion of the metallic particles was partly but not fully melted.

As in the HVOF, the dwell time and the process temperature were lower than in APS, less phase transformation of the elements to the oxide status occurred (XRD in Fig. 4). These transformations determine the macroscopic properties of the coating such as hardness, porosity, and surface roughness. As discussed, the coating microstructure could be influenced by the mechanism of droplet impact on the substrate and solidification conditions (Ref 40). In some systems, the surrounding gas can be trapped under the impacting droplet (Ref 40).

3.1.3 HVAF-Sprayed Coatings. SEM micrographs of the Ni, NiCr, and NiAl coatings in Fig. 5, 6, and 7, respectively, prove that although there are some variations in coatings' porosity generally all coatings look dense and compact. Defects like vertical or horizontal cracks are not common in the coating microstructure. The micrographs show that the coatings processing has been performed in a good way and initially chosen parameters are in a practically acceptable range.

There were some clear differences among the microstructures of HVAF, HVOF, and APS coatings. The HVAF coatings depicted a denser appearance compared to APS- and HVOF-sprayed coatings owing to the higher velocity and lower temperature of the in-flight particles.

Therefore, the HVAF coatings represented a lower melting state and lower extent of oxidation than HVOF and APS coating. Less oxidation on lamellar boundaries can be detected in HVAF compared to HVOF and APS coatings due to the lower particle temperature during spraying. Higher lamellar cohesion was also obvious in HVAF coatings. Lowering the particle temperature in HVAF might have negative influence on the cohesive strength of the coating, which, despite its low oxygen content, might not provide maximal corrosion resistance (Ref 41). However, the SEM analysis at high magnification showed a very good contact between the particles that may reveal a good cohesion among the melted particles inside the coatings.

3.2 XRD

Comparison of the obtained XRD diffraction peaks from the powders and optimized coatings in Fig. 4 shows that the NiCr and NiAl coatings seem to retain the powder chemistry and microstructure, proving that no undesired reactions occurred at high processing temperatures of the three spraying techniques. It can be generally concluded that the amount and types of the phases in the coatings were the same as the powders and the characteristics of the powders were preserved during the processing. As the

Table 5 HVAF spraying process parameters for NiCr

Coatings	Nozzle	Air pressure, MPa	Fuel 1 pressure (propane), MPa	Fuel 2 pressure (propane), MPa	Powder carrier gas (N ₂) flow, L/min	Feed rate, g/min	Pass velocity, m/min	Pass spacing, mm/rev.	Thickness per pass, μm	Number of cycles	SoD, mm
NiCr1	4L2G	0.8	0.69	0.69	60	150	100	5	28.3	6	300
NiCr2	4L4G	0.83	0.69	0.69	60	150	100	5	33.3	6	300
NiCr3	4L2G	0.8	0.69	0.69	60	75	100	5	18.8	13	350
NiCr4	4L2G	0.8	0.69	0.69	60	75	100	5	19.2	13	300
NiCr5	4L2G	0.8	0.69	0.69	60	75	100	5	19.2	13	250

Table 6 HVAF spraying process parameters for NiAl

Coatings	Nozzle	Air pressure, MPa	Fuel 1 pressure (propane), MPa	Fuel 2 pressure (propane), MPa	Powder carrier gas (N ₂) flow, L/min	Feed rate, g/min	Pass velocity, m/min	Pass spacing, mm/rev.	Thickness per pass, μm	Number of cycles	SoD, mm
NiAl1	4L2G	0.8	0.69	0.69	60	150	100	5	33.7	8	300
NiAl2	3L2G	0.8	0.68	0.69	60	150	100	5	34.3	7	300
NiAl3	3L2G	0.8	0.68	0.69	60	75	100	5	15.7	15	300
NiAl4	3L2G	0.8	0.68	0.69	60	75	100	5	16.8	14	350
NiAl5	3L2G	0.8	0.68	0.69	60	75	100	5	17.3	15	250

optimized coatings were selected for XRD analysis, no oxidation of Cr and Al was detected in all coating processes.

Phase identification of XRD patterns in the Ni coatings revealed the presence of NiO in APS, while there was no sign of oxides in HVAF and HVOF, which in turn demonstrates the high reliability of the two processes to produce the pure Ni coatings. It is pertinent to mention that the oxide content of the coating is significantly influenced by the process parameters, i.e., changes in the in-flight particle characteristics including velocity and temperature. The lower particle velocity and higher particle temperature in APS compared to HVOF and HVAF imply that the in-flight particles spend longer time in the high-temperature flame exposed to oxygen, which results in higher oxide content in the APS coatings (Ref 42).

3.3 Microhardness Investigation

Hardness of the coating is an important property that can significantly affect the functional performances of the coating under different types of wear conditions (Ref 43). Thus, it is important to determine the processing factors, which can give the desired hardness of the coating. Result of hardness measurements is given in Table 7. All of the HVAF coatings had higher hardness compared to the corresponding coatings produced by the two other techniques. An important point is that, although a relatively large range of HVAF spray parameters were used to deposit the coatings, most of the coatings exhibited high hardness values with low scattering. This means that these powders were insensitive to the variations of temperature and velocity of the flame, which is beneficial for industrial applications. A lower deviation from the mean values of the hardness in HVAF coatings stands for higher homo-

geneity of well-distributed material phases and defects compared to the HVOF and APS coatings, which eventually contributes to better corrosion resistance of the HVAF coating (Ref 44). All APS-sprayed coatings exhibited lower hardness values than those sprayed with the HVOF or HVAF processes.

3.4 Effect of the Process Parameters in the HVAF Process

The cross-sectional microstructure of the coatings underwent changes when the SoD and feed rate were changed (Fig. 5, 6, and 7). Among the Ni coatings, the Ni1 coating sprayed with SoD of 300 mm and feed rate of 150 mm/min showed the least porosity. Among the NiCr coatings, the NiCr5 sample (SoD of 250 mm and feed rate of 75 mm/min) exhibited the least porous structure. As regard the NiAl coatings, the NiAl2 coating (SoD of 300 mm and feed rate of 150 mm/min) showed the least porous microstructure. At these configurations, the particle seems to reach the optimum velocity and temperature when impinging the surface, leading to a balance of impact, flattening, and solidification. At other configurations in the Ni and NiAl coatings, the coating exhibited a larger amount of pores (Table 7). Changing the configuration, some particles may re-solidify before reaching substrate resulting in a coating with high amount of partially molten or re-molten particles, which implicitly led to a slight increment in the porosity.

It is pertinent to mention that contributing one single process variable or a set of them to the final coating properties is meaningless. Indeed, the coating properties and performance are governed by the coating process as a whole.

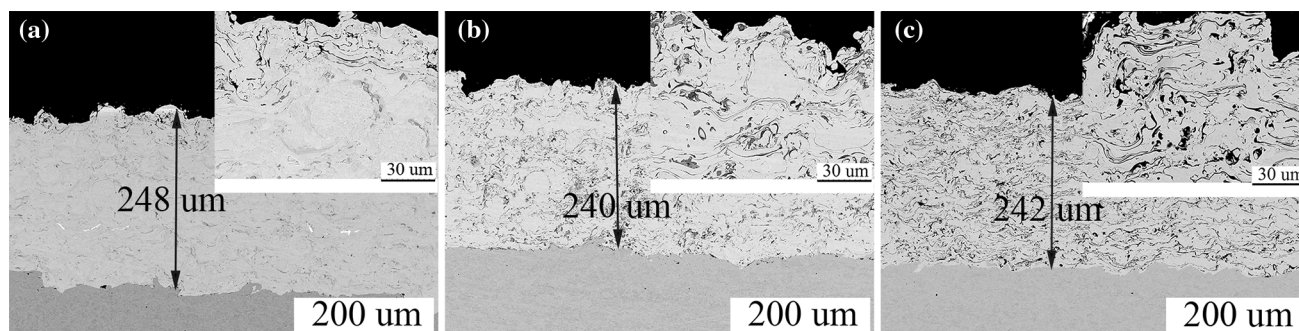


Fig. 2 Back-scattered cross-sectional SEM micrographs of APS-sprayed coatings, (a) Ni, (b) NiCr, and (c) NiAl

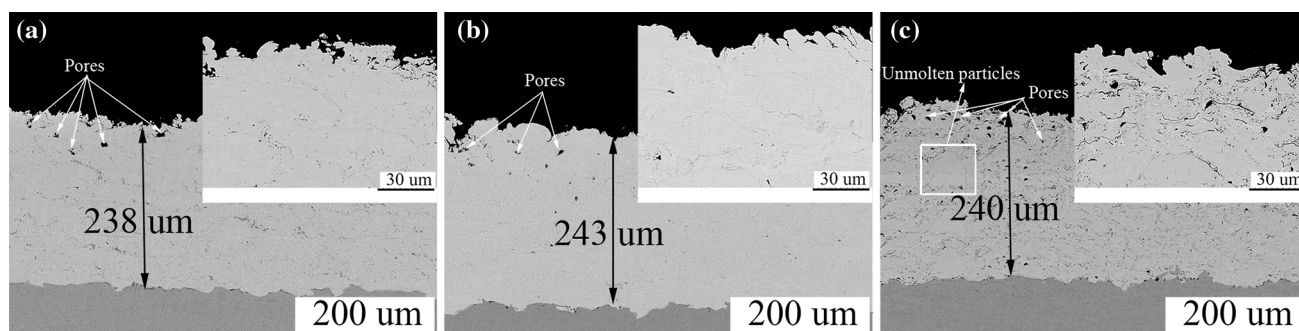


Fig. 3 Back-scattered cross-sectional SEM micrographs of HVOF-sprayed coatings, (a) Ni, (b) NiCr, and (c) NiAl

The results proved that the coating's chemical composition needs to be considered carefully once the optimized process parameters are going to be selected. For instance, a slight change in the spraying distance affects the substrate temperature, dwell time, and characteristics of the powder particles in the jet stream. Indeed, different configurations result in different in-flight particle velocities and temperatures when impacting the substrate. Typically, short SoDs allow the particles to reach the substrate with high temperature and high velocity (Ref 45). Indeed, increasing the powder feed rate and shortening the SoD together lead to the higher deposition temperature and higher particles impingement at high velocities. The microstructure of the coating is the result of having mainly partially melted particles that might result in high level of porosity (Ref 46). The impact of particles at high velocity may lead to debonding of splats in the splat surfaces during deposition.

The obtained hardness values confirmed the porosity results, i.e., APS coatings were more porous than the HVOF and HVAF coatings. Due to the low in-flight particle velocity and high operating temperature of the APS system, the powder particles experienced larger heat loads during the flight resulting in higher porosity in the coating (according to the mechanism presented above). The presence of pores in the coatings contributed to lowering the hardness values of the coatings (Ref 47, 48). The average value of the hardness in the HVOF coatings compared to the APS and HVAF coatings can be associated with the average in-flight particle velocity and temperature, porosity, and degree of phase transformation.

3.5 Coating Roughness Measurements

Table 7 provides the coating roughness values measured on the coatings investigated in this work. Surface roughness is important in corrosion protection applications, as lower surface roughness results in a lower surface area exposed to a corrosive solution, which can lead to lower susceptibility to both general and localized corrosion (Ref 49). Lower roughness of the as-sprayed NiCr coatings produced by HVAF ($\approx 4.3 \mu\text{m}$) presented lower susceptibility to the above-mentioned types of corrosion compared to the NiAl and Ni coatings. It is pertinent to mention that there was no direct connection between the spraying processes and the surface roughness of the sprayed coatings. APS coatings are indeed produced by fully molten particles, which flatten extensively upon impact and form lamellae; hence, the surface is reasonably expected to be smoother than that of HVAF samples, which, though being the densest, are built-up of particles that never flatten completely, being often just at the melting point at impact, and retain a partly curved shape, particularly because the final layer of particles was never peened by the next ones impacting on top of them. The R_a values of the APS-sprayed NiAl and APS-sprayed Ni were lower than the equal coatings produced by HVAF, whereas the R_a values were lower in HVAF-sprayed NiCr coating compared to the APS NiCr coating.

As pointed out above, one of the most important requirements in corrosion protection is to avoid porosity in coating corrosion resistant films (Ref 50, 51). The relationship between the surface roughness and the initiation

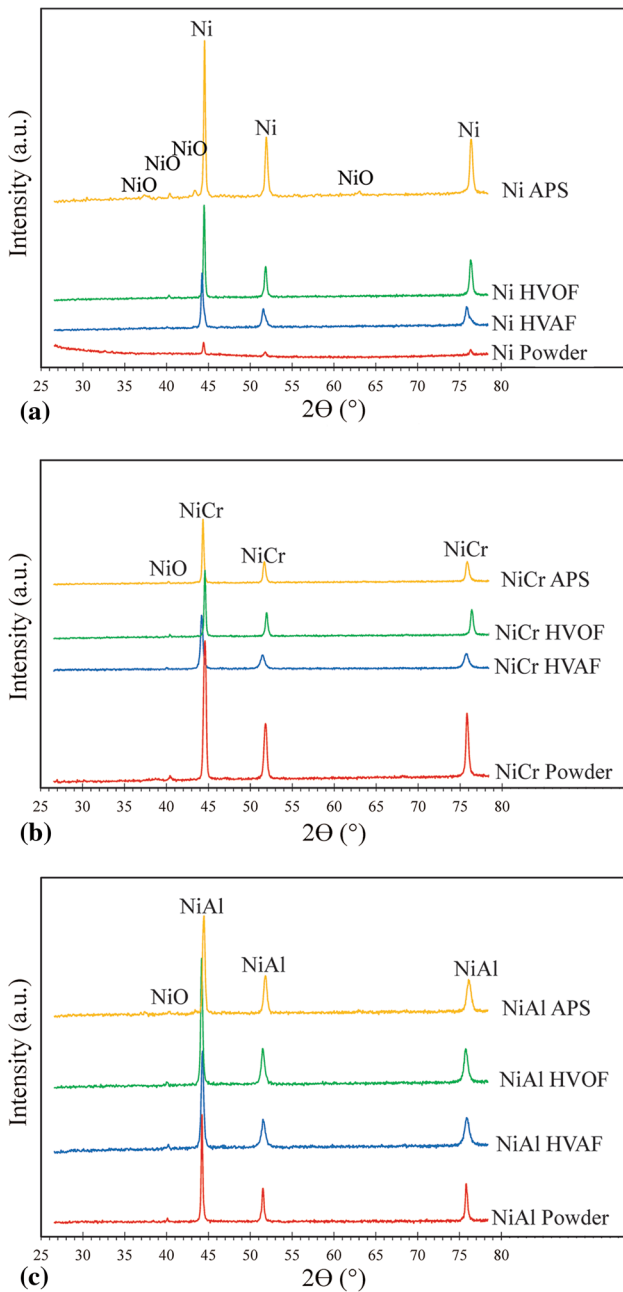


Fig. 4 XRD patterns of the powders and corresponding as-sprayed APS, HVOF, and HVAF coatings, (a) Ni, (b) NiCr, and (c) NiAl

of pitting was studied elsewhere (Ref 42), and it was found that as the arithmetical mean deviation (R_a) decreased, the porosity decreased accordingly. It was also shown in the other study that the corrosion rate increased with an increase in the surface roughness (Ref 52). The current density in the sharp peaks and valleys was by far higher than at the middle of the hole, so that the summit of peaks and end of the holes would corrode faster. An increase in roughness might also support the formation of corrosion cells that could further accelerate the corrosion of the rough surface (Ref 53).

3.6 Corrosion Behavior

3.6.1 Open-Circuit Potential (OCP). Figure 8 shows the OCP values of APS-, HVOF- and HVAF-sprayed coatings studied over 3 h in 3.5 wt.% NaCl solution. All coatings gained a steady potential after around 2.5 h of immersion. The HVAF coatings showed the higher OCP value compared to HVOF and APS coatings, confirming the more uniform microstructure of HVAF coatings with less defects, e.g., pores, lamella boundaries, and surface cracks.

Frequent potential oscillations of the OCP curves showed the influence of Cr and Al elements in the chemical composition of the coating on their corrosion behavior. The fluctuations showed the capability of the coatings to passivation and depassivation in the corrosive environment to control the corrosion. On the other hand, the irregular formation of the passive layer increases the susceptibility of the coatings to localized corrosion, in particular pitting in the chlorine environment (Ref 36). Therefore, Fig. 8 shows that the Cr in the NiCr coatings is capable of providing higher corrosion potential than the Al in the NiAl coatings. The OCP values of the NiCr coatings varied from -0.2 (NiCr5) to -0.47 (NiCr-P) V/SEC, whereas the OCP of all NiAl coatings remained around -0.32 V/SEC. The results showed that the tendency of the NiAl coatings to corrosion was not affected by altering the spraying processes. The NiCr coatings showed a wider range of the OCP values; however, NiCr with the optimized HVAF process parameters (NiCr5) could lead to higher OCP values than the NiAl coatings. It also illustrated that the NiCr coating microstructure was strongly affected by spraying processes and corresponding microstructure. The OCP of all coatings decreased with time in the active direction at the onset of the immersion. The drop can be attributed to changes in the surface activity due to the penetration of electrolyte through the coating pores or dissolution of the initial oxide layer that probably formed on the coating surface in air during sample preparation (Ref 54).

3.6.2 Polarization Resistance. Figure 9 shows the potentiodynamic polarization plots of the APS-, HVOF- and HVAF-sprayed coatings tested in 3.5 wt.% NaCl at 25 °C. All the electrochemical parameters derived from the potentiodynamic polarization plots shown in Fig. 9 are given in Table 8. The results not only verified that the HVAF coatings presented a better corrosion performance than the HVOF and APS coatings, but also confirmed that the NiCr coatings showed better corrosion protection than the NiAl coatings in NaCl solution due to the better ability of Cr to form a more stable passive layer that protects the samples (Ref 55, 56). The lower corrosion current density (i_{corr}) and higher corrosion potential (E_{corr}) given in Table 8 illustrated that the HVAF coatings were able to provide a better protection compared to the other coatings. Interconnected pores and oxides in the splat boundaries of the HVOF and APS coatings are detrimental to the corrosion resistance of the coatings because corrosive elements can infiltrate through the coating (Ref 57-59). A dense and homogenous structure like the HVAF

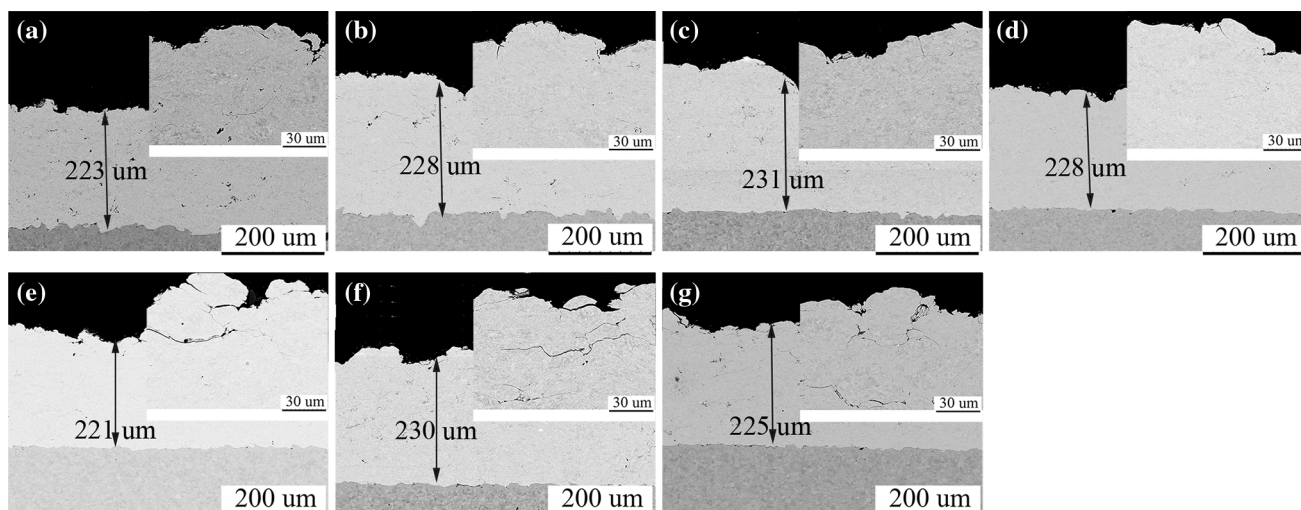


Fig. 5 Back-scattered cross-sectional SEM micrographs of HVAF-sprayed Ni coatings, (a) Ni1, (b) Ni2, (c) Ni3, (d) Ni4, (e) Ni5, (f) Ni6, and (g) Ni7

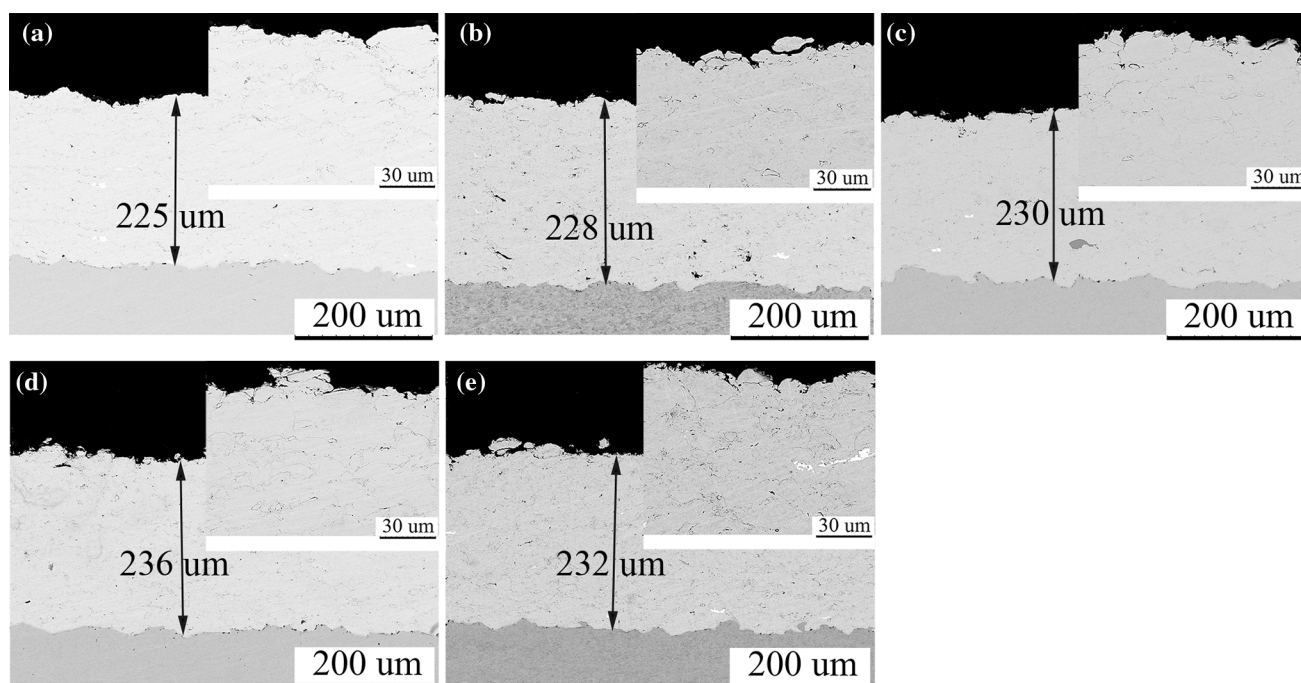


Fig. 6 Cross-sectional SEM micrographs of HVAF-sprayed NiCr coatings, (a) NiCr1, (b) NiCr2, (c) NiCr3, (d) NiCr4, and (e) NiCr5

coatings is essential for corrosion resistance of the coating, and thus, special attention should be paid on optimization of spray parameters (Ref 60, 61). When an optimized dense coating structure is achieved, the need for post-treatments such as laser re-melting, heat treatment, sealing, or the unwanted coating breakdown during usage can be avoided. The APS- and HVOF-sprayed coatings containing more oxides, and pores were unable to show a better performance than the homogenous HVAF coatings, confirming the adverse influence of the defects on the corrosion behavior. This means that these coatings were not as suc-

cessful in preventing the solution from penetrating to the substrate as the HVAF coatings are. The results in Table 8 show that the HVAF-sprayed NiCr coatings presented a better corrosion performance, kinetically and thermodynamically, due to their lower i_{corr} and higher E_{corr} , respectively, compared to the Ni and NiAl coatings.

Based on the results presented in Table 8, it was found that the process parameters such as SoD and feed rate have marked effects not only on the produced microstructure but also on the corrosion behavior of the HVAF-sprayed coatings.

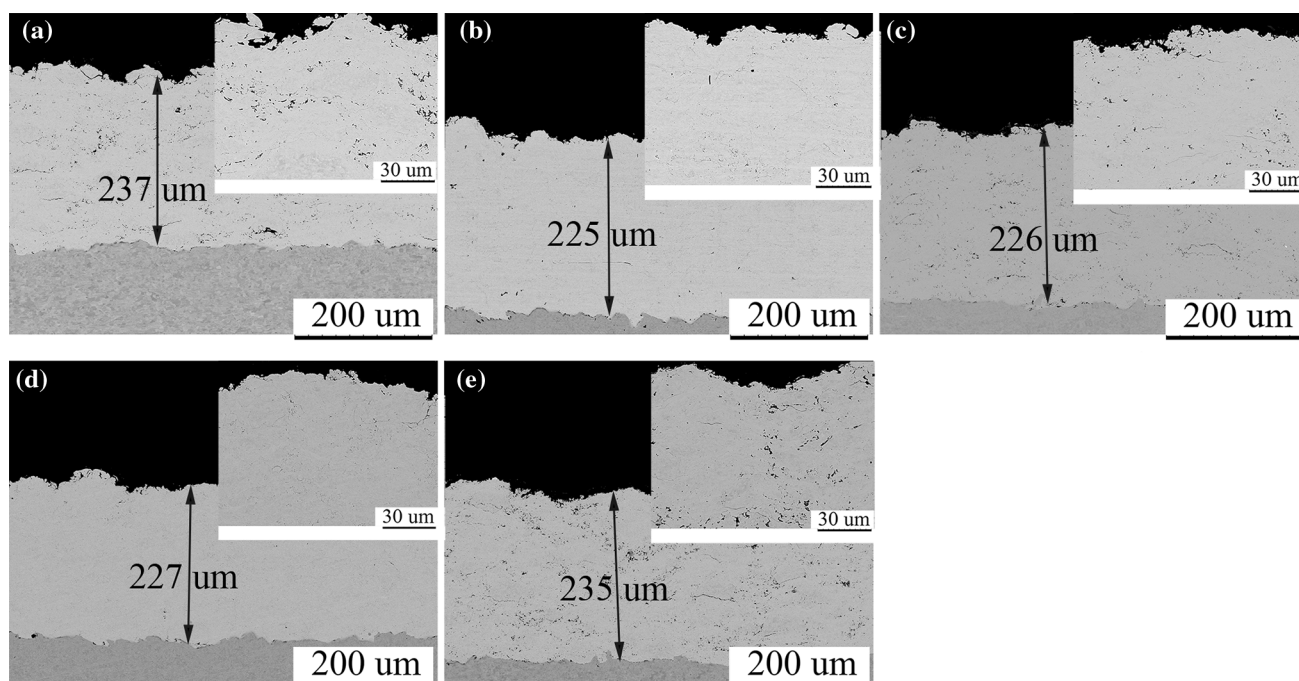


Fig. 7 Cross-sectional SEM micrographs of HVAF-sprayed NiAl coatings, (a) NiAl1, (b) NiAl2, (c) NiAl3, (d) NiAl4, and (e) NiAl5

Table 7 Thicknesses, surface roughness, hardness, and pore content of as-sprayed coatings

Coatings	Thickness, μm	Roughness, R_a , μm	Hardness, $\text{HV}_{0.3}$	Porosity, vol. %
Ni-O	238 ± 9	8.3 ± 0.4	212 ± 12	0.9 ± 0.05
Ni-P	248 ± 11	7.3 ± 0.5	187 ± 10	1.7 ± 0.1
Ni				
1	223 ± 7	8.9 ± 0.3	244 ± 11	0.1 ± 0.01
2	228 ± 7	9.0 ± 0.3	242 ± 10	0.9 ± 0.05
3	231 ± 7	9.1 ± 0.3	233 ± 10	0.5 ± 0.02
4	228 ± 6	8.5 ± 0.2	232 ± 9	0.7 ± 0.03
5	221 ± 6	8.3 ± 0.2	234 ± 9	0.4 ± 0.02
6	230 ± 7	8.8 ± 0.2	211 ± 8	0.2 ± 0.01
7	225 ± 7	8.4 ± 0.2	228 ± 10	0.2 ± 0.01
NiCr-O	243 ± 10	9.7 ± 0.5	255 ± 13	1.6 ± 0.1
NiCr-P	240 ± 12	7.5 ± 0.6	205 ± 13	3.2 ± 0.2
NiCr				
1	225 ± 9	3.9 ± 0.2	421 ± 18	0.4 ± 0.02
2	228 ± 7	4.5 ± 0.3	403 ± 17	0.9 ± 0.05
3	230 ± 9	4.3 ± 0.2	361 ± 15	0.8 ± 0.05
4	236 ± 10	4.5 ± 0.2	387 ± 16	1.0 ± 0.06
5	232 ± 12	4.4 ± 0.2	416 ± 16	0.3 ± 0.01
NiAl-O	240 ± 11	7.4 ± 0.5	324 ± 16	2.3 ± 0.2
NiAl-P	242 ± 13	6.0 ± 0.5	191 ± 11	5.5 ± 0.4
NiAl				
1	237 ± 8	7.2 ± 0.4	434 ± 21	1.4 ± 0.4
2	225 ± 7	6.4 ± 0.3	407 ± 19	0.1 ± 0.01
3	226 ± 6	6.8 ± 0.3	421 ± 20	2.0 ± 0.5
4	227 ± 6	6.8 ± 0.3	403 ± 17	0.2 ± 0.04
5	235 ± 9	7.2 ± 0.4	428 ± 21	0.8 ± 0.05

Figure 10 shows the SEM micrographs of the cross section of APS, HVOF, and HVAF NiCr coatings after polarization tests, where no sign of blistering or delamination of the coatings can be observed. The APS and HVOF coatings seem to be locally attacked in some areas

on the surface and also inside the coating (noted as arrows in Fig. 10), whereas the corrosion damage in the HVAF coating is less. No visible microcracks were detected in the HVAF coating. The attacked areas were confined essentially at the base of the microcracks as shown by white

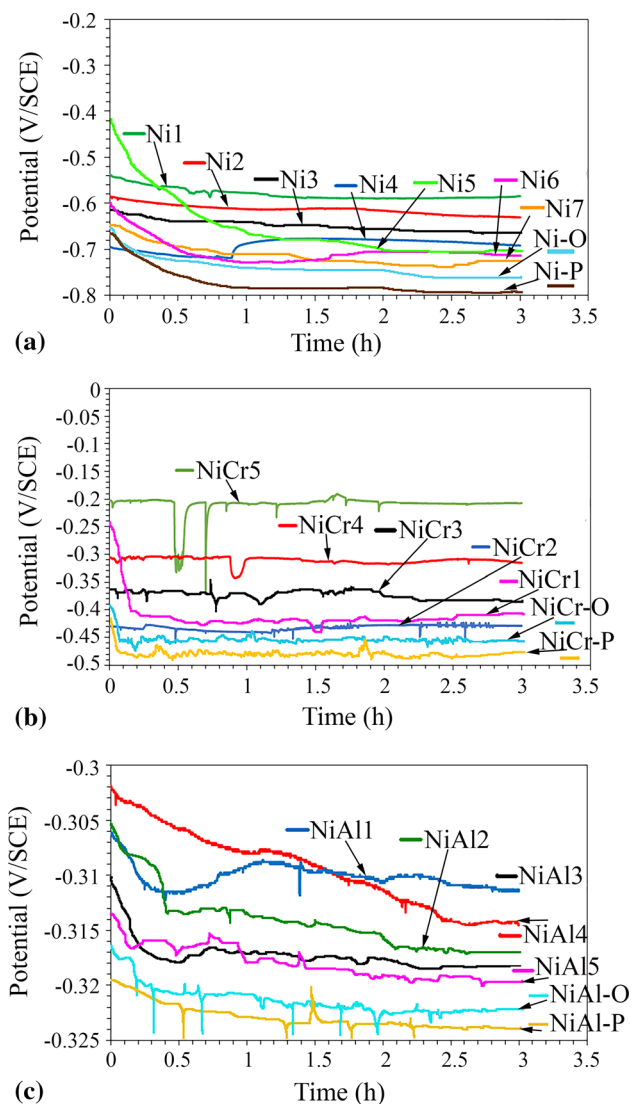


Fig. 8 OCP of the APS-, HVOF-, and HVAF-sprayed coatings over 3 h in the 3.5 wt.% NaCl solution, (a) Ni, (b) NiCr, and (c) NiAl coatings

arrows in Fig. 10. The microcracks are favorable sites for microgalvanic and/or microcrevice corrosion of thermal spray coatings as reported in the literature (Ref 36). As previously discussed, faster diffusion of tiny Cl^- ions than that of oxygen occurring in these regions can limit the passive behavior of the coatings. In order to characterize the attacked regions of the coatings, EDS point analysis was performed. The depletion of Ni element in the APS and HVOF coatings (compared to the chemistry of the as-received powders) at these sites confirmed the local dissolution of Ni from these areas. In addition, the presence of oxygen may be due to oxidation of Ni (identified by XRD analysis) during the corrosion process. These results verified that the HVAF coating with less porosity compared to the other two techniques provided better corrosion behavior.

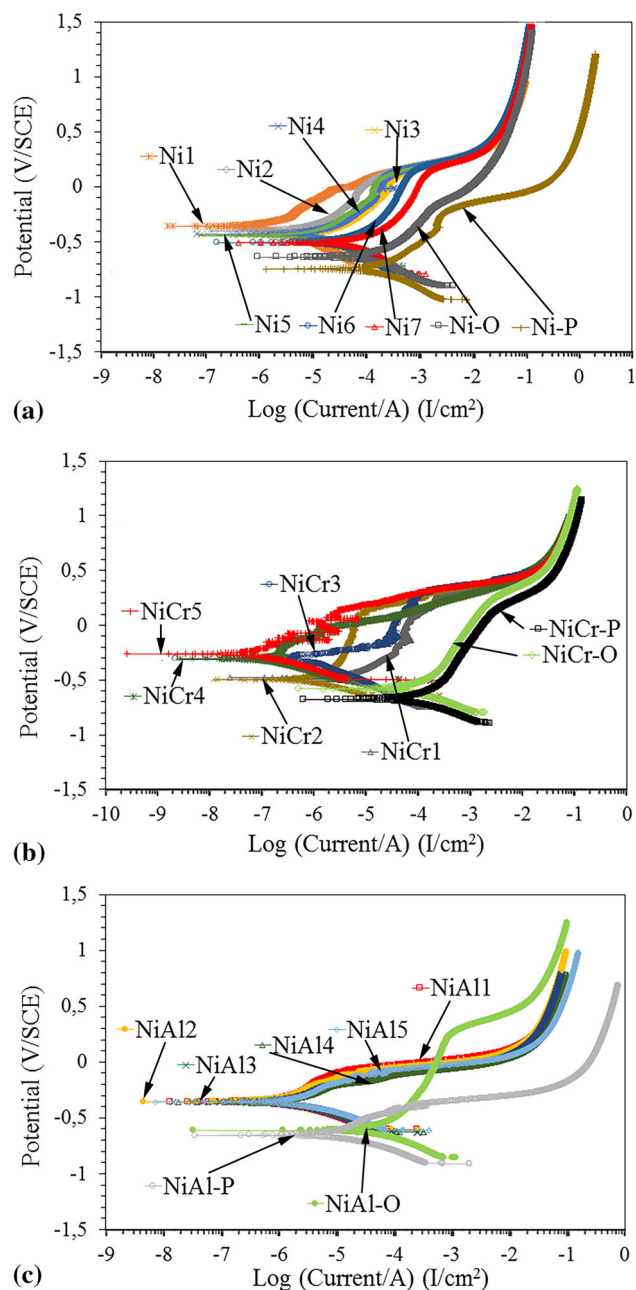


Fig. 9 Potentiodynamic polarization plots of the APS-, HVOF-, and HVAF-sprayed coatings, (a) Ni, (b) NiCr, and (c) NiAl coatings. All specimens were immersed in 3.5 wt.% NaCl, at 25 °C (at a scan rate of 1.0 mV/s)

4. Conclusions

The APS-, HVOF- and HVAF-sprayed Ni, NiCr and NiAl coatings were investigated in terms of microstructure, porosity, roughness, and hardness values as well as corrosion resistance. The corrosion behavior of the HVAF coatings was compared with the previously optimized APS- and HVOF-sprayed coatings. The main conclusions drawn from the investigation can be summarized as follows:

Table 8 Electrochemical values of the coated steel substrate, immersed in 3.5 wt.% NaCl at 25 °C

Coatings	i_{corr} , $\mu\text{A}/\text{cm}^2$	E_{corr} , V versus SCE	β_{a} , V/dec	β_{c} , V/dec	R_{p}^{a} , $\text{k}\Omega \text{ cm}^2$
Ni-O	6.1 ± 0.4	-0.65 ± 0.03	0.35 ± 0.02	0.11 ± 0.005	6 ± 0.3
Ni-P	18.8 ± 0.9	-0.73 ± 0.05	0.38 ± 0.02	0.12 ± 0.005	2 ± 0.9
Ni					
1	0.12 ± 0.05	-0.36 ± 0.03	0.08 ± 0.04	0.05 ± 0.002	111 ± 6
2	0.78 ± 0.04	-0.40 ± 0.04	0.29 ± 0.02	0.28 ± 0.01	79 ± 4
3	1.2 ± 0.06	-0.44 ± 0.02	0.25 ± 0.02	0.13 ± 0.008	31 ± 4
4	0.97 ± 0.05	-0.43 ± 0.02	0.24 ± 0.02	0.17 ± 0.009	45 ± 3
5	0.68 ± 0.03	-0.45 ± 0.02	0.23 ± 0.02	0.12 ± 0.009	50 ± 3
6	2.47 ± 0.1	-0.51 ± 0.03	0.25 ± 0.02	0.09 ± 0.001	12 ± 0.7
7	4.97 ± 1.3	-0.51 ± 0.03	0.36 ± 0.03	0.14 ± 0.001	9 ± 0.6
NiCr-O	1.4 ± 0.08	-0.63 ± 0.03	0.15 ± 0.01	0.09 ± 0.001	17 ± 1.1
NiCr-P	3.2 ± 1.2	-0.70 ± 0.04	0.08 ± 0.01	0.07 ± 0.003	5 ± 0.3
NiCr					
1	0.33 ± 0.015	-0.48 ± 0.03	0.22 ± 0.01	0.11 ± 0.009	96 ± 5
2	0.03 ± 0.016	-0.50 ± 0.03	0.09 ± 0.01	0.08 ± 0.005	613 ± 33
3	0.04 ± 0.016	-0.31 ± 0.01	0.16 ± 0.02	0.14 ± 0.008	810 ± 42
4	0.003 ± 0.001	-0.30 ± 0.01	0.04 ± 0.01	0.02 ± 0.005	1929 ± 98
5	0.002 ± 0.001	-0.26 ± 0.01	0.08 ± 0.01	0.06 ± 0.005	7443 ± 645
NiAl-O	0.5 ± 0.03	-0.62 ± 0.03	0.26 ± 0.01	0.09 ± 0.007	58 ± 3
NiAl-P	0.8 ± 0.04	-0.68 ± 0.04	0.21 ± 0.02	0.07 ± 0.003	29 ± 2
NiAl					
1	0.02 ± 0.005	-0.36 ± 0.02	0.09 ± 0.01	0.05 ± 0.004	697 ± 35
2	0.04 ± 0.007	-0.35 ± 0.02	0.07 ± 0.01	0.04 ± 0.005	276 ± 13
3	0.03 ± 0.007	-0.36 ± 0.01	0.06 ± 0.01	0.03 ± 0.004	289 ± 15
4	0.02 ± 0.007	-0.36 ± 0.02	0.08 ± 0.01	0.05 ± 0.004	668 ± 31
5	0.03 ± 0.006	-0.36 ± 0.02	0.06 ± 0.01	0.05 ± 0.003	394 ± 29

^a R_{p} measured based on Stern-Geary equation

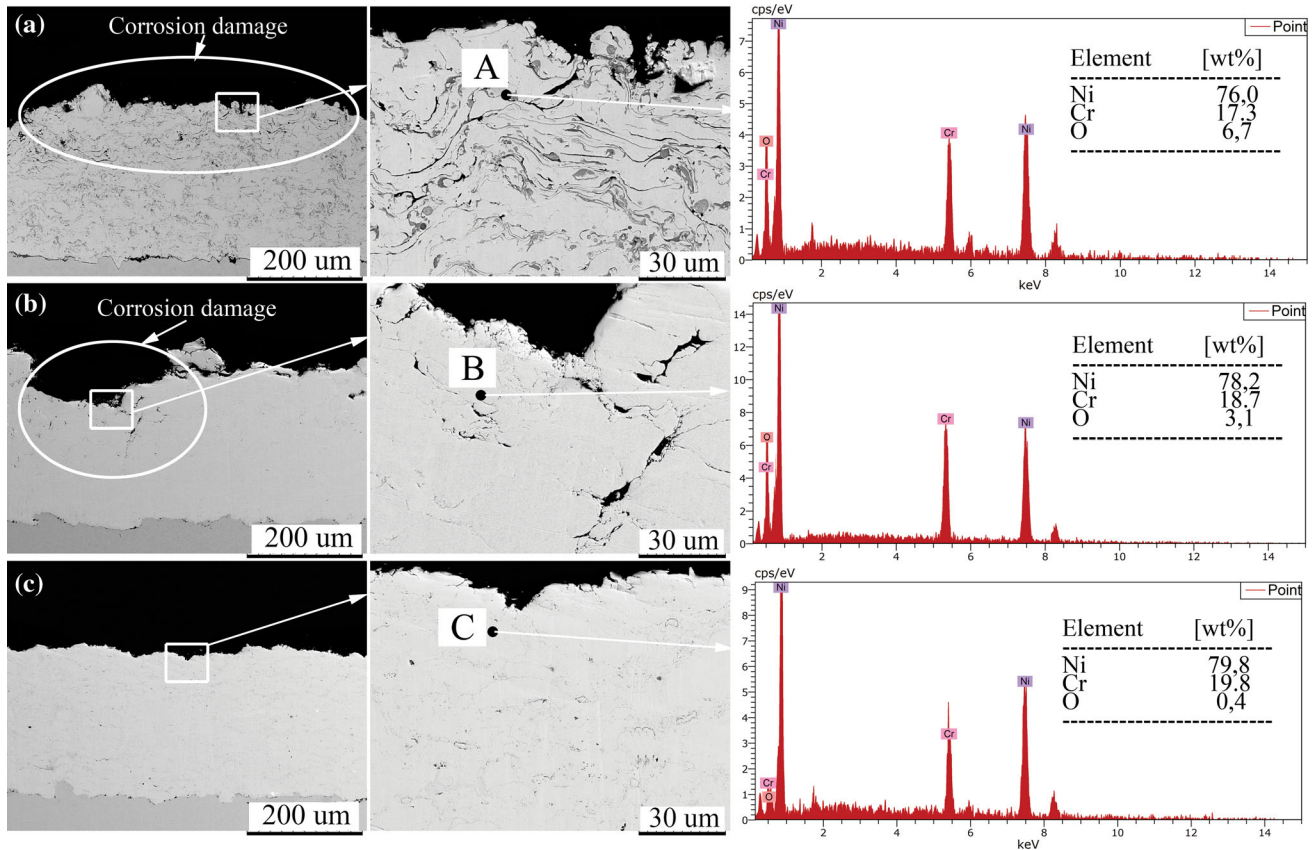


Fig. 10 Cross-sectional SEM micrographs of the corroded NiCr coatings sprayed with different techniques and the corresponding EDS point analysis, (a) APS, (b) HVOF, and (c) HVAF



1. Significant microstructural differences were observed for the coatings sprayed with the same chemistry but different spraying techniques. No visible pores or microcracks were detected in the HVOF coatings, while the pores and microcracks were evidently observed in the other two spraying techniques, in particular APS.
 2. The HVOF process presented better coating characteristics and corrosion behavior compared to the APS and HVOF processes for Ni, NiCr, and NiAl in 3.5 wt.% NaCl solution at ambient temperature.
 3. The Ni and NiAl coatings with the least porosity were obtained at SoD of 300 mm with high feed rate of 150 g/min in the HVOF process. Changing the process configuration led either to excessive flattening of splats or to un-molten condition, resulting in high levels of porosity, accordingly low polarization resistance (R_p).
 4. Results showed that the APS-sprayed coatings comprising more diffusion paths for passive layer-forming elements such as Cr^{2+} or Al^{3+} could not tolerate the corrosive environment better than the dense HVOF coatings.
 5. The presence of cathodic sites (Ni binder) adjacent to anodic sites (Al or Cr) in the NiCr and NiAl coatings increased the corrosion effects.
 6. Cr in the NiCr coating provided a better passivation behavior compared to Al in the NiAl coating in the studied test conditions.
 7. The corrosion behavior of the coatings produced by different techniques can be explained in terms of the microstructural differences. In the case APS and HVOF, microcracks and interlamellar boundaries were responsible for the quick electrolyte penetration into the coatings, whereas the dense HVOF coating microstructure enhanced the corrosion resistance.
4. D. Srinivasan, V. Chandrasekhar, R. Amuthan, Y.C. Lau, and E. Calla, Characterization of Cold-Sprayed IN625 and NiCr Coatings, *J. Therm. Spray Technol.*, 2016, **25**, p 725-744
 5. D. Ward et al., Functional NiAl-Graphene Oxide Composite as a Model Coating for Aerospace Component Repair, *Carbon*, 2016, **105**, p 529-543
 6. H. Koivuluoto, A. Milanti, G. Bolelli, L. Lusvardi, and P. Vuoristo, High-Pressure Cold-Sprayed Ni and Ni-Cu Coatings: Improved Structures and Corrosion Properties, *J. Therm. Spray Technol.*, 2013, **23**(1-2), p 98-103
 7. M. Akhtari Zavareh, A.A.D. Mohammed Sarhan, P. Akhtari Zavareh, and W.J. Basirun, Electrochemical corrosion behavior of carbon steel pipes coated with a protective ceramic layer using plasma and HVOF thermal spray techniques for oil and gas, *Ceram. Int.*, 2016, **42**(2, Part B), p 3397-3406
 8. M. Akhtari Zavareh, A.A.D.M. Sarhan, B.B. Razak, and W.J. Basirun, The Tribological and Electrochemical Behavior of HVOF-Sprayed Cr₃C₂-NiCr Ceramic Coating on Carbon Steel, *Ceram. Int.*, 2015, **41**(4), p 5387-5396
 9. J.A.C. Miramontes, J.Y.A. Calahorra, A.T. Estrada, G.P. Baulto, C.P. Salas, and F.A. Calderon, Evaluation of the Electrochemical Behavior in Acid Media of HVOF-Spray Alloy Coatings, *ECS Trans.*, 2015, **64**(26), p 81-87
 10. A. Niaz and M.S. Bakare, Electrochemical corrosion testing and characterization of potential assisted passive layer on HVOF Inconel 625 coating, *Corros. Rev.*, 2015, **33**(1-2), p 63-76
 11. S.D. Zhang, W.L. Zhang, S.G. Wang, X.J. Gu, and J.Q. Wang, Characterisation of Three-Dimensional Porosity in an Fe-Based Amorphous Coating and Its Correlation with Corrosion Behaviour, *Corros. Sci.*, 2015, **93**, p 211-221
 12. P. Fauchais and A. Vardelle, Thermal Sprayed Coatings Used Against Corrosion and Corrosive Wear. *Advanced Plasma Spray Applications*, H. Jazi, Ed., INTECH Open Access Publisher, 2012
 13. X. Gong, H. Peng, Y. Ma, H. Guo, and S. Gong, Microstructure Evolution of an EB-PVD NiAl Coating and Its Underlying Single Crystal Superalloy Substrate, *J. Alloys Compd.*, 2016, **672**, p 36-44
 14. Y. Itoh and M. Tamura, Reaction Diffusion Behaviors for Interface Between Ni-Based Super Alloys and Vacuum Plasma Sprayed MCrAlY Coatings, *J. Eng. Gas Turbines Power*, 1999, **121**(3), p 476-483
 15. M. Aghasibeig, M. Mousavi, F.B. Ettouill, C. Moreau, R. Wuthrich, and A. Dolatabadi, Electrocatalytically Active Nickel-Based Electrode Coatings Formed by Atmospheric and Suspension Plasma Spraying, *J. Therm. Spray Technol.*, 2013, **23**(1-2), p 220-226
 16. J. Porcayo-Calderon, O. Sotelo-Mazon, A. Luna-Ramirez, E. Porcayo-Palafox, V.M. Salinas-Bravo, and L. Martinez-Gomez, Electrochemical Behavior of NiAl and Ni₃Al Intermetallic Coatings in 1.0 M NaOH Solution, *Int. J. Electrochem. Sci.*, 2015, **10**(8), p 6241-6256
 17. A.P. Wang, Z.M. Wang, J. Zhang, and J.Q. Wang, Deposition of HVOF-Sprayed Ni-Based Amorphous Metallic Coatings, *J. Alloys Compd.*, 2007, **440**(1-2), p 225-228
 18. E. Sadeghimeresht, N. Markocsan, and P. Nylén, A Comparative Study of Corrosion Resistance for HVOF-Sprayed Fe- and Co-Based Coatings, *Coatings*, 2016, **6**, p 16
 19. S. Matthews, B. James, and M. Hyland, High Temperature Erosion-Oxidation of Cr₃C₂-NiCr Thermal Spray Coatings Under Simulated Turbine Conditions, *Corros. Sci.*, 2013, **70**, p 203-211
 20. E. Sadeghimeresht, N. Markocsan, and P. Nylén, HVOF Thermal Spray Fe-Based Coating: An Environmentally Acceptable Alternative to Cobalt-Based Coating. Presented at the EUROCORR 2015, EUROPEAN CORROSION CONGRESS 6-10 September 2015 Graz/Austria The annual event of the European Federation of Corrosion, 2015
 21. C. Clement, E. Sadeghimeresht, C. Lyphout, N. Markocsan, and P. Nylén, Corrosion Behavior of HVOF- and HVOF-sprayed High-Chromium Fe-Based Coatings. Presented at the 7th Rencontres Internationales sur la Projection Thermique, 9th to 11th December 2015—Limoges, France, 2015

Acknowledgments

The authors would like to express their acknowledgment to Mr. Jonas Olsson, Mr. Kenneth Andersson, Mr. Björn Kjellman, and Mr. Jan Wigren for their advice in processing, engineering, and developing of the HVOF, APS, and HVOF thermal spray experimental work in this study.

References

1. L. Ajdelsztajn, B. Jodoin, and J.M. Schoenung, Synthesis and Mechanical Properties of Nanocrystalline Ni Coatings Produced by Cold Gas Dynamic Spraying, *Surf. Coat. Technol.*, 2006, **201**(3-4), p 1166-1172
2. C. Lyphout, A. Fasth, and P. Nylén, Mechanical Property of HVOF Inconel 718 Coating for Aeronautic Repair, *J. Therm. Spray Technol.*, 2013, **23**(3), p 380-388
3. P.L. Fauchais, J.V.R. Heberlein, and M.I. Boulos, Industrial Applications of Thermal Spraying Technology. *Thermal Spray Fundamentals*, P.L. Fauchais, Ed., Springer US, New York, 2014, p 1401-1566

22. Q. Wang, S. Zhang, Y. Cheng, J. Xiang, X. Zhao, and G. Yang, Wear and Corrosion Performance of WC-10Co4Cr Coatings Deposited by Different HVOF and HVAF Spraying Processes, *Surf. Coat. Technol.*, 2013, **218**, p 127-136
23. G. Bolelli et al., Tribology of HVOF- and HVAF-Sprayed WC-10Co4Cr Hardmetal Coatings: A Comparative Assessment, *Surf. Coat. Technol.*, 2015, **265**, p 125-144
24. G. Bolelli et al., Sliding and Abrasive Wear Behaviour of HVOF- and HVAF-Sprayed Cr3C2-NiCr Hardmetal Coatings, *Wear*, 2016, **358-359**, p 32-50
25. G. Bolelli et al., Tribological Behavior of HVOF- and HVAF-Sprayed Composite Coatings Based on Fe-Alloy + WC-12% Co, *Surf. Coat. Technol.*, 2014, **248**, p 104-112
26. H.R. Ma et al., Wear Resistance of Fe-Based Amorphous Coatings Prepared by AC-HVAF and HVOF. *Mater. Sci. Technol.*, 2016, **32**, p 1-7
27. Y. Li, Y. Lian, J. Cao, and L. Li, Solid Particle Erosion Behavior of HVOF/HVAF Sprayed WC-Co-Cr Coatings. *Proc. Inst. Mech. Eng. Part J J. Eng. Tribol.*, 2015, **230**, p 1350650115608209
28. I. Hulka, V.A. Serban, I. Secosan, P. Vuoristo, and K. Niemi, Wear Properties of CrC-37WC-18M Coatings Deposited by HVOF and HVAF Spraying Processes, *Surf. Coat. Technol.*, 2012, **210**, p 15-20
29. L. Pawlowski, *The Science and Engineering of Thermal Spray Coatings*. John Wiley & Sons, 2008
30. C.-J. Li and G.-J. Yang, Relationships Between Feedstock Structure, Particle Parameter, Coating Deposition, Microstructure and Properties for Thermally Sprayed Conventional and Nanostructured WC-Co, *Int. J. Refract. Met. Hard Mater.*, 2013, **39**, p 2-17
31. R.S. Lima and B.R. Marple, Process-Property-Performance Relationships for Titanium Dioxide Coatings Engineered From nanostructured and Conventional Powders, *Mater. Des.*, 2008, **29**(9), p 1845-1855
32. C. Lyphout et al., Tribological Properties of Hard Metal Coatings Sprayed by High-Velocity Air Fuel Process, *J. Therm. Spray Technol.*, 2015, **25**(1-2), p 331-345
33. ASTM B276-05(2015), *Standard Test Method for Apparent Porosity in Cemented Carbides*. ASTM International, West Conshohocken, PA, 2015, www.astm.org
34. ASTM E384-16, *Standard Test Method for Microindentation Hardness of Materials*. ASTM International, West Conshohocken, PA, 2016, www.astm.org
35. U. Angst and M. Büchler, On the Applicability of the Stern-Geary Relationship to Determine Instantaneous Corrosion Rates in Macro-cell Corrosion, *Mater. Corros.*, 2015, **66**(10), p 1017-1028
36. M.M. Verdian, K. Raeissi, and M. Salehi, Corrosion Performance of HVOF and APS Thermally Sprayed NiTi Inter-metallic Coatings in 3.5% NaCl Solution, *Corros. Sci.*, 2010, **52**(3), p 1052-1059
37. S. Sampath, X.Y. Jiang, J. Matejcek, L. Prechlik, A. Kulkarni, and A. Vaidya, Role of Thermal Spray Processing Method on the Microstructure, Residual Stress and Properties of Coatings: An Integrated Study for Ni-5 wt.%Al Bond Coats, *Mater. Sci. Eng., A*, 2004, **364**(1-2), p 216-231
38. S. Deshpande, S. Sampath, and H. Zhang, Mechanisms of Oxidation and Its Role in Microstructural Evolution of Metallic Thermal Spray Coatings—Case Study for Ni-Al, *Surf. Coat. Technol.*, 2006, **200**(18-19), p 5395-5406
39. S. Kuroda, Y. Tashiro, H. Yumoto, S. Taira, H. Fukunuma, and S. Tobe, Peening Action and Residual Stresses in High-Velocity Oxygen Fuel Thermal Spraying of 316L Stainless Steel, *J. Therm. Spray Technol.*, 2001, **10**(2), p 367-374
40. S. Chandra and P. Fauchais, Formation of Solid Splats During Thermal Spray Deposition, *J. Therm. Spray Technol.*, 2009, **18**(2), p 148-180
41. S. Matthews, B. James, and M. Hyland, The Role of Microstructure in the Mechanism of High Velocity Erosion of Cr₃C₂-NiCr Thermal Spray Coatings: Part 2—Heat Treated Coatings, *Surf. Coat. Technol.*, 2009, **203**(8), p 1094-1100
42. S. Al-Mutairi, M.S.J. Hashmi, B.S. Yilbas, and J. Stokes, Microstructural Characterization of HVOF/Plasma Thermal Spray of Micro/Nano WC-12%Co Powders, *Surf. Coat. Technol.*, 2015, **264**, p 175-186
43. J.R. Davis, *Handbook of Thermal Spray Technology*. ASM International, 2004
44. E. Sadeghimeresht, N. Markocsan, P. Nylén, and S. Björklund, Corrosion Performance of Bi-Layer Ni/Cr2C3-NiCr HVAF Thermal Spray Coating, *Appl. Surf. Sci.*, 2016, **369**, p 470-481
45. C. Lyphout, S. Björklund, M. Karlsson, M. Runte, G. Reisel, and P. Boccaccio, Screening Design of Supersonic Air Fuel Processing for Hard Metal Coatings, *J. Therm. Spray Technol.*, 2014, **23**(8), p 1323-1332
46. G. Wang, Z. Huang, P. Xiao, and X. Zhu, Spraying of Fe-Based Amorphous Coating with High Corrosion Resistance by HVAF, *J. Manuf. Process.*, 2016, **22**, p 34-38
47. R.S. Lima, A. Kucuk, and C.C. Berndt, Evaluation of Microhardness and Elastic Modulus of Thermally Sprayed Nanostructured Zirconia Coatings, *Surf. Coat. Technol.*, 2001, **135**(2-3), p 166-172
48. S. Liu, X. Zheng, and G. Geng, Dry Sliding Wear Behavior and Corrosion Resistance of NiCrBSi Coating Deposited by Activated Combustion-High Velocity Air Fuel Spray Process, *Mater. Des.*, 2010, **31**(2), p 913-917
49. T. Hong and M. Nagumo, Effect of Surface Roughness on Early Stages of Pitting Corrosion of Type 301 Stainless Steel, *Corros. Sci.*, 1997, **39**(9), p 1665-1672
50. S. Liscano, L. Gil, and M.H. Staia, Effect of Sealing Treatment on the Corrosion Resistance of Thermal-Sprayed Ceramic Coatings, *Surf. Coat. Technol.*, 2004, **188-189**, p 135-139
51. P.K. Aw, A.L.K. Tan, T.P. Tan, and J. Qiu, Corrosion Resistance of Tungsten Carbide Based Cermet Coatings Deposited by High Velocity Oxy-Fuel Spray Process, *Thin Solid Films*, 2008, **516**(16), p 5710-5715
52. B. Yoo, K.R. Shin, D.Y. Hwang, D.H. Lee, and D.H. Shin, Effect of Surface Roughness on Leakage Current and Corrosion Resistance of Oxide Layer on AZ91Mg Alloy Prepared by Plasma Electrolytic Oxidation, *Appl. Surf. Sci.*, 2010, **256**(22), p 6667-6672
53. S. Picard, J.B. Memet, R. Sabot, J.L. Grosseau-Poussard, J.P. Rivière, and R. Meilland, Corrosion Behaviour, Microhardness and Surface Characterisation of Low Energy, High Current Ion Implanted Austenitic Stainless Steel, *Mater. Sci. Eng., A*, 2001, **303**, p 163-172
54. J.B. Cheng, X.B. Liang, and B.S. Xu, Effects of Crystallization on the Corrosion Resistance of Arc-Sprayed FeBSiNb Coatings, *J. Therm. Spray Technol.*, 2013, **23**(3), p 373-379
55. Z. Zhou, L. Wang, F. Wang, and Y. Liu, Formation and Corrosion Behavior of Fe-Based Amorphous Metallic Coatings Prepared by Detonation Gun Spraying, *Trans. Nonferrous Met. Soc. China*, 2009, **19**(Supplement 3), p s634-s638
56. G. Bolelli, R. Giovanardi, L. Lusvardi, and T. Manfredini, Corrosion Resistance of HVOF-Sprayed Coatings for Hard Chrome Replacement, *Corros. Sci.*, 2006, **48**(11), p 3375-3397
57. M. Campo et al., Corrosion Resistance of Thermally Sprayed Al and Al/SiC Coatings on Mg, *Surf. Coat. Technol.*, 2009, **203**(20-21), p 3224-3230
58. M. Carboneras et al., Corrosion Behaviour of Thermally Sprayed Al and Al/SiCp Composite Coatings on ZE41 Magnesium Alloy in Chloride Medium, *Corros. Sci.*, 2010, **52**(3), p 761-768
59. A. Lekatou, D. Zois, and D. Grimalis, Corrosion Properties of HVOF Cermet Coatings with Bond Coats in an Aqueous Chloride Environment, *Thin Solid Films*, 2008, **516**(16), p 5700-5705
60. C. Taltavull, A.J. Lopez, B. Torres, A. Atrens, and J. Rams, Optimisation of the High Velocity Oxygen Fuel (HVOF) Parameters to Produce Effective Corrosion Control Coatings on AZ91 Magnesium Alloy, *Mater. Corros.*, 2015, **66**(5), p 423-433
61. Y. Qin et al., Optimization of the HVOF Spray Parameters by Taguchi Method for High Corrosion-Resistant Fe-Based Coatings, *J. Mater. Eng. Perform.*, 2015, **24**(7), p 2637-2644